

Near-Infrared Luminescence in Trinuclear Mixed-Metal Chalcogenolate Complexes of the Types $[M_2Ti(EPh)_6(PPh_3)_2]$ ($M = Cu, Ag; E = S, Se$) and $[Na(thf)_3]_2[Ti(SPh)_6]$

Sergei Lebedkin, Florian Weigend, and Andreas Eichhöfer*

Cite This: <https://doi.org/10.1021/acs.inorgchem.1c00829>

Read Online

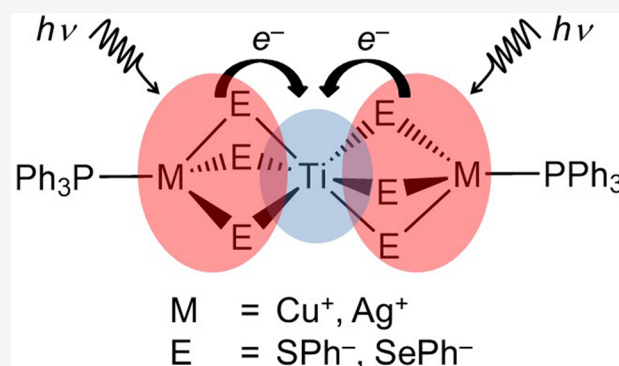
ACCESS |

Metrics & More

Article Recommendations

Supporting Information

ABSTRACT: The optical properties of four new trinuclear chalcogenolato bridged metal complexes $[Ag_2Ti(SPh)_6(PPh_3)_2]$, $[Na(thf)_3]_2[Ti(SPh)_6]$, $[Cu_2Ti(SePh)_6(PPh_3)_2]$, and $[Ag_2Ti(SePh)_6(PPh_3)_2]$ have been investigated by absorption and photoluminescence spectroscopy as well as time-dependent density functional theory (TDDFT) calculations and compared to the results published recently for $[Cu_2Ti(SPh)_6(PPh_3)_2]$. All of these compounds are distinguished by efficient near-infrared luminescence at ~ 880 – 1200 nm in the solid state at low temperatures, which remains quite intense for the copper–titanium complexes at ambient temperature with PL quantum yields of 9.5 and 4.8% at $\lambda_{PL} = 1090$ and 1240 nm for $[Cu_2Ti(EPh)_6(PPh_3)_2]$, $E = S, Se$, respectively. According to the calculations, a peculiar feature of the lowest-energy electronic transitions in these complexes is their high localization on the metal and chalcogen atoms, with negligible contributions of the “external” ligand groups. Correspondingly, the type of atoms in the M_2TiE_6 ($M = Cu, Ag, Na$) core structure determines optical properties such as the absorption and emission wavelengths and PL lifetime.



INTRODUCTION

Copper(I) complexes with a high luminescence efficiency (up to $\sim 90\%$ in the solid state at ambient temperature) have been evaluated as potential materials for future economical and mass-producible organic light-emitting diodes (OLEDs)^{1,2} and light-emitting electrochemical cells (LECs).^{3,4} In particular, numerous multimetallic copper-based complexes, also including cluster compounds, have been found to show bright photoluminescence (PL).^{5–14} Depending on the specific complex structure, the PL (typically phosphorescence or delayed fluorescence) has been observed across the whole visible range from blue to deep red, demonstrating various electronic relaxation and decay patterns in the solid state and solution. In most of these compounds, photoexcitation results in the initial charge “separation” via metal-to-ligand charge transfer (MLCT) transitions which are often followed by intersystem crossing (ISC) leading to long-lived triplet excited states.

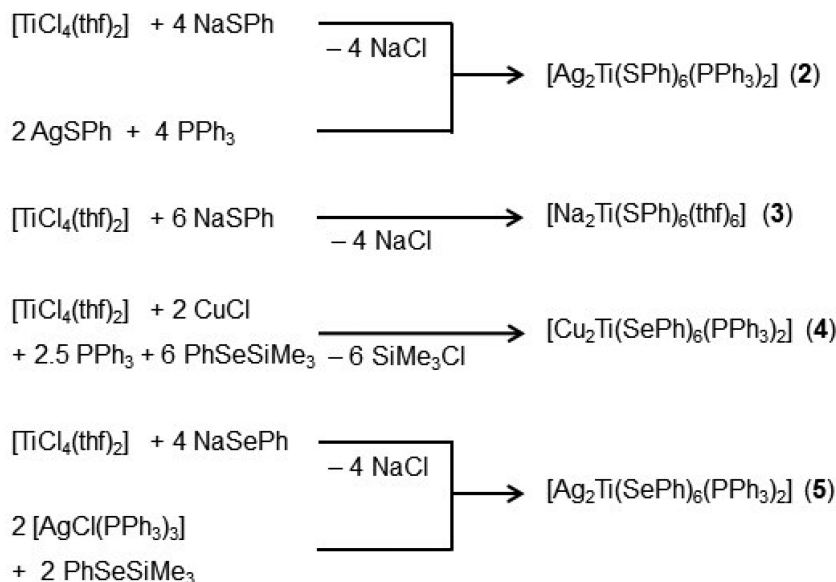
In a recent work, the emission range of copper-based complexes has been extended up to the near-infrared (NIR) by introducing ternary copper chalcogenolato complexes $[Cu_2M'(EPh)_6(PPh_3)_2]$ ($M' = Sn, Ti; E = S, Se$) which comprise additional tin or titanium atoms in the copper chalcogen framework and emit at ~ 700 – 1100 nm in the solid state.^{15,16} Furthermore, $[Cu_2Ti(SPh)_6(PPh_3)_2]$ retains an

efficient emission at ~ 1100 nm at ambient temperature with a quantum yield of 9.5%. Time-dependent density functional theory (TDDFT) calculations revealed that in this case the electronic transitions from a mixture of filled sulfur p and copper d orbitals into empty titanium d or tin s orbitals dominate the lowest-energy absorptions.¹⁵ As examples of structure-related compounds, one can also mention the heteroheptanuclear Sn(IV)–Cu(I) oxosulphur complex $[Sn_3Cu_4(S_2C_2H_4)_6(\mu_3-O)(PPh_3)_4](ClO_4)_2$ which generates blue-green light at 495 nm¹⁷ and the large cluster complex $(NBu_4)[Cu_{19}S_{28}(SnPh)_{12}(PEt_2Ph)_3]$ demonstrating a deep-red PL at 820 nm below $T \approx 100$ K (decreasing in intensity and shifting to ~ 930 nm at 200 K).¹⁸

Despite the great diversity of luminescence properties found for copper-based complexes, the above examples of NIR emitters beyond 950 nm—in the spectral region of interest, for instance, for biological imaging and telecommunication—remain, to our knowledge, very rare. Such emitters, especially

Received: March 17, 2021

Scheme 1. Synthesis Reactions for 2–5



those with relatively high PL quantum yields, are also quite rare among other transition-metal complexes. In the field of molecular NIR emitters, one usually relies on suitable lanthanide derivatives.^{19–21} It is worth noting that a chalcogen framework can be advantageously used for the synthesis of complexes and clusters of NIR-luminescent lanthanides, as has been demonstrated by Brennan and co-workers.^{22,23} However, although NIR emission is ubiquitous for lanthanide complexes, it is still usually of poor efficiency,²⁴ in part as a general consequence of the emission energy gap law predicting the enhanced competition of nonradiative decay with NIR emission.^{25,26}

The above considerations justify interest in the extraordinary PL properties of $[\text{Cu}_2\text{Ti}(\text{SPh})_6(\text{PPh}_3)_2]$ (1). In a subsequent work, we have found that the copper atoms can be readily replaced in this structure with silver or sodium. In addition, selenium can be introduced instead of sulfur. In the following text, we report on four new trinuclear complexes: $[\text{Ag}_2\text{Ti}(\text{EPh})_6(\text{PPh}_3)_2]$ (E = S (2), Se (5)), $[\text{Na}(\text{thf})_3]_2[\text{Ti}(\text{SPh})_6]$ (3), and $[\text{Cu}_2\text{Ti}(\text{SePh})_6(\text{PPh}_3)_2]$ (4) (Scheme 1), which luminesce at NIR wavelengths of as long as ~880–1240 nm. We describe in detail the synthesis, crystallographic data, and absorption and emission spectra as well as the results of modeling these spectra within TDDFT calculations.

RESULTS AND DISCUSSION

Syntheses and Structures. The synthesis and structural data have already been published for 1.²⁷ Syntheses of 2–5 have been performed by using related reactions shown in Scheme 1. In the solid (polycrystalline) state, all of these compounds appear to be deeply colored, from dark violet-red to almost black.

Single-crystal X-ray analysis reveals that compounds 1–5 crystallize in the same trigonal space group $R\bar{3}$ with similar lattice constants (Tables S1 and S2 in the Supporting Information (SI)).²⁸ The structures of 1, 2, 4, and 5 are depicted in Scheme 2 and Figures S1–S3, and that of 3 in Figure 1. The main structural parameters of 1–5 are compared in Table 1.

Scheme 2. Structures of Complexes 1, 2, 4, and 5

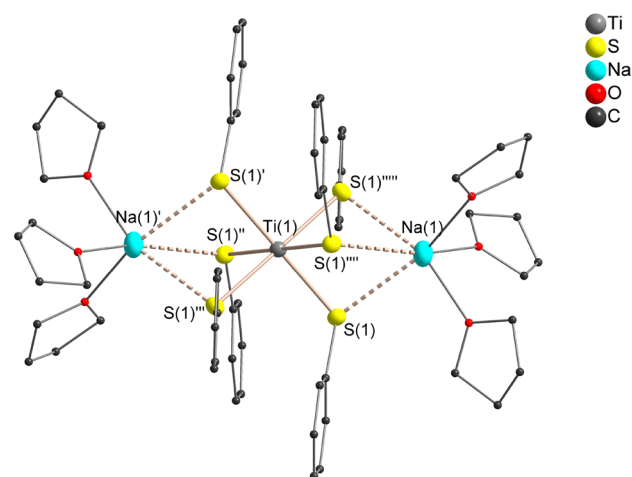
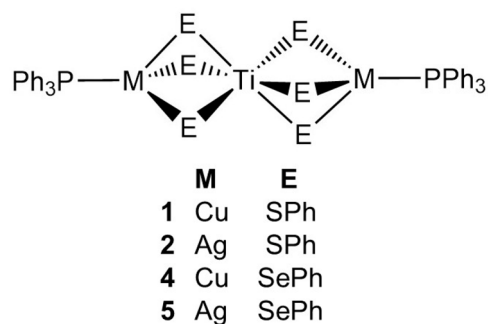


Figure 1. Molecular structure of $[\text{Na}(\text{thf})_3]_2[\text{Ti}(\text{SPh})_6]$ (3) (H atoms are omitted for clarity). Thermal ellipsoid plots at 50% probability. For selected bond lengths and angles, see Table 1. Symmetry transformation for the generation of equivalent atoms: $'4/3 - x, 2/3 - y, 2/3 - z; ''1/3 - y + x, -1/3 + x, 2/3 - z; ''1/3 + y, 2/3 - x + y, 2/3 - z; ''''1 + y - x, 1 - x, +z; ''''1 - y, x - y, +z$.

In each structure, there is an inversion center at the titanium atom and a 3-fold rotational axis which runs through the linear chains formed by the $\text{M}^{1+} = \text{Cu}, \text{Ag}, \text{Na}, \text{titanium}$, and

Table 1. Selected Bond Distances (pm) and Angles (deg) of $[\text{Cu}_2\text{Ti}(\text{SPh})_6(\text{PPh}_3)_2]$ (1), $[\text{Ag}_2\text{Ti}(\text{SPh})_6(\text{PPh}_3)_2]$ (2), $[\text{Na}(\text{thf})_3]_2[\text{Ti}(\text{SPh})_6]$ (3), $[\text{Cu}_2\text{Ti}(\text{SePh})_6(\text{PPh}_3)_2]$ (4), and $[\text{Ag}_2\text{Ti}(\text{SePh})_6(\text{PPh}_3)_2]$ (5)

	M	E	Ti–E (pm)	E–Ti–E (deg)	M–E (pm)	M–E–Ti (deg)	M–Ti (pm)
1	Cu	S	246.27(6)	86.98(2), 93.03(2)	235.28(6)	71.10(2)	280.11(5)
2	Ag	S	244.86(7)	88.01(2), 92.00(2)	261.10(8)	77.88(2)	318.24(4)
3	Na	S	244.69(4)	84.69(1), 95.31(1)	296.47(10)	89.00(2)	381.11(13)
4	Cu	Se	258.53(3)	88.86(1), 91.14(1)	244.26(4)	67.24(1)	278.65(6)
5	Ag	Se	258.00(4)	89.06(1), 90.94(1)	269.07(5)	74.99(2)	320.96(6)

phosphorus atoms. In terms of polyhedral coordination, the molecular structures of 1–5 can be viewed as consisting of a distorted octahedrally coordinated titanium atom sharing parallel trigonal faces with two copper/silver-centered “ME₃P” (M = Cu, Ag; E = S, Se) tetrahedrons or sodium-centered NaS₃O₃ octahedrons, respectively. Different structural parameters for 1–5 reflect the different elements involved (Table 1). The quite similar and only slightly distorted TiE₆ octahedral coordination spheres display for the structures with bridging selenium atoms (4, 5) roughly 10 pm longer Ti–E bond distances in comparison to those with sulfur atoms (1–3). A similar observation can be made for the M–E bonds in the complexes with M = Cu, Ag (1, 2, 4, and 5). However, the Na–S bond distance in 3 is 296.47 pm and distinctly longer than the other four M–E bonds due to its more ionic character. Another important geometrical parameter is the M–E–Ti bond angle which is most acute in 4 (67.24°) and increases further up to 89.00° in the order of 1 < 5 < 2 < 3. In combination, the different M–E bond distances and M–E–Ti bond angles produce a varying M–Ti distance which is, with a distinct gap, the longest in 3 (381.11 pm) and decreases in the other complexes from 320.96 pm down to 278.65 pm in the order of 5 > 2 > 1 > 4. We note that the observed increase in M–Ti bond distances is not directly reflected by the change in the ionic radii of the metals Cu (77 pm), Ag (115 pm), and Na (102 pm).

Assuming the phenyl-chalcogenolato ligands –SPh and –SePh to be singly negatively charged, we assign, in agreement with previous reports, the formal oxidation states of +IV to the titanium atoms and +I to the coinage metal as well as sodium atoms.^{27,15} In the literature, several other heterobimetallic trinuclear complexes can be found, which comprise a similar linear metal skeleton, including $[\text{Cu}_2\text{Sn}(\text{EPh})_6(\text{PPh}_3)_2]$ (E = S, Se),^{15,16} $[\text{Ag}_2\text{Sn}(\text{SPh})_6(\text{PPh}_3)_2]$,¹⁵ $[\text{Cu}_2\text{Nb}(\text{SePh})_6(\text{PR}_3)_2]$ (R = org. group),²⁹ $[\text{Co}_2\text{V}(\text{SPh})_8]^{2-}$, $[\text{Ni}_2\text{V}(\text{SPh})_8]^{2-}$,³⁰ $[\text{Cu}_2\text{M}(\text{SAr})_6(\text{PPh}_3)_2]$ (M = W, Mo, U; Ar = Ph, *p*-C₆H₄Me, *p*-C₆H₄F, *p*-C₆H₄Cl, *p*-C₆H₄Br),^{31–33} and $[\text{LFeMFeL}]^{n+}$ (M = Ge, Sn; *n* = 2, 3; L = 1,4,7-(4-*tert*-butyl-2-mercaptobenzyl)-1,4,7-triazacyclononane).³⁴

The measured powder X-ray diffraction (XRD) patterns of 1–5 show good agreement with the calculated ones based on the single-crystal data (Figures S4–S8), which proves the crystalline purity of the samples used for optical spectroscopy. Slightly increasing differences in the position of the peaks with increasing detection angle arise from the temperature difference between data collections (single-crystal XRD at 180 K vs powder XRD at room temperature).

Photophysical Properties: Experiment and Theory. Absorption spectra of powdered crystals of 1–5 were measured in transmission and reflection modes using an integrating sphere at 295 K, whereas their PL excitation (PLE) and emission spectra were obtained in the temperature range of 5–295 K (Figures 2, 3, and S9–S11).³⁵ Experimental Stokes

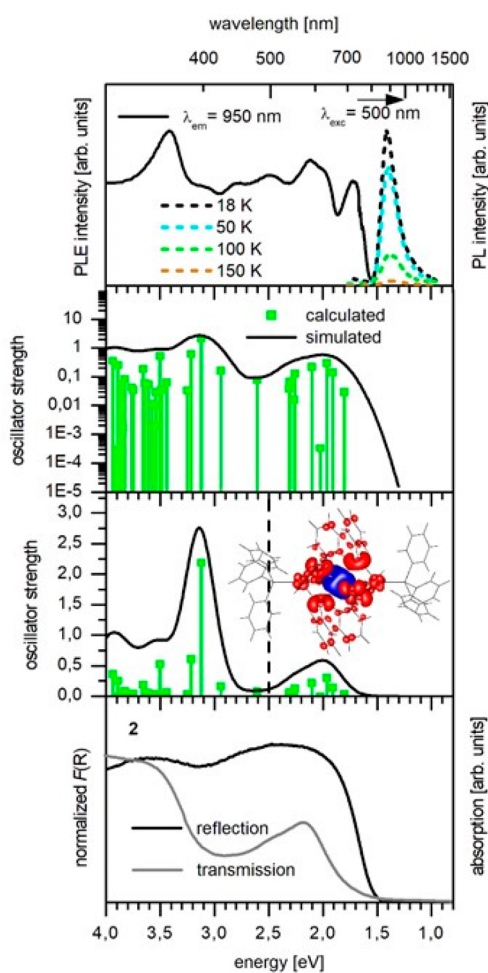


Figure 2. Summary of the experimental (powdered crystals in mineral oil) and calculated (TDDFT) electronic spectra of $[\text{Ag}_2\text{Ti}(\text{SPh})_6(\text{PPh}_3)_2]$ (2). (Top) Photoluminescence excitation (PLE, solid line) and emission (PL, dashed line) at different temperatures. (Middle) Calculated singlet excitation energies and oscillator strengths plotted as vertical lines (green) as well as superimposed Gaussians of fwhm = 0.3 eV (black curve) for simulation on normal and log scales. The character of the peaks (up to 2.5 eV) is visualized using the nonrelaxed transition densities. (See the text.) The contributions of occupied orbitals are plotted in red, and those of the unoccupied orbitals in blue. (Bottom) UV–vis–NIR in transmission and reflection modes at room temperature.

shifts (SS) were estimated for 1–5 from the PLE and PL spectra at low temperatures as the energetic difference in the first PLE and the PL maximum (Table 2, Figure S11). The spectra of newly prepared 1 corresponded well to those in ref 15.

Singlet excitation energies were calculated within TDDFT using the experimental (single-crystal XRD) structural

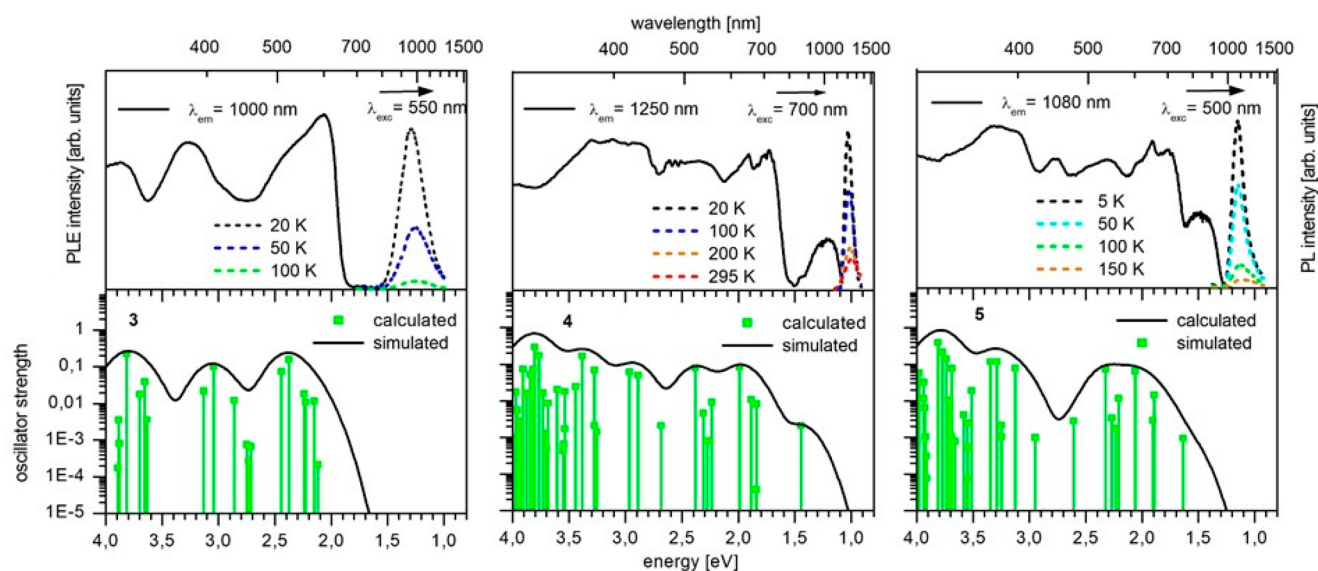


Figure 3. Summary of the experimental (powdered crystals in mineral oil) and calculated (TDDFT) electronic spectra of $[\text{Na}(\text{thf})_3][\text{Ti}(\text{SPh})_6]$ (3), $[\text{Cu}_2\text{Ti}(\text{SePh})_6(\text{PPh}_3)_2]$ (4), and $[\text{Ag}_2\text{Ti}(\text{SePh})_6(\text{PPh}_3)_2]$ (5) (left, middle, and right panels, respectively). (Top) Photoluminescence excitation (PLE, solid line) and emission (PL, dashed line) at different temperatures. (Bottom) Calculated singlet excitation energies and oscillator strengths plotted as vertical lines (green) as well as superimposed Gaussians with $\text{fwhm} = 0.3$ eV (black curve) for simulation on a log scale.

Table 2. PL and PLE Data from Experiment^a

	$\lambda_{\text{PLE}}/E_{\text{PLE}}$ 20 K	$\lambda_{\text{PL}}/E_{\text{PL}}$ 20 K	$\lambda_{\text{PL}}/E_{\text{PL}}$ 150 K	ΔE_{SS} 20 K ^b	τ , 20 K
1	875/1.42	1063/1.17	1090/1.14 ^c	0.25	0.04
2	720/1.72	885/1.40	920/1.35	0.32	9.1, 3.2 (50:50) ^d
3	602/2.06	960/1.29	955/1.30	0.77	24, 6.1 (78:22) ^d
4	1030/1.20	1205/1.03	1240/1.00 ^b	0.17	0.052
5	840/1.48	1075/1.15 ^c	1100/1.13	0.33 ^d	0.09 ^d

^aFirst photoluminescence excitation maximum $\lambda_{\text{PLE}}/E_{\text{PLE}}$ (nm/eV) (Figure S11), photoluminescence emission wavelength λ_{PL} (nm), and energy E_{PL} (eV), Stokes shift ΔE_{SS} (eV), and decay time τ (μs) for 1–5. ^b $\Delta E_{\text{SS}} = E_{\text{PLE}} - E_{\text{PL}}$. ^cValues at 295 K. ^dBiexponential decay parameters with relative amplitudes of two exponential components in brackets. The averaged lifetimes correspond to 6.1 and 20 μs for 2 and 3, respectively. ^eValues at 5 K.

parameters, as well as the optimized molecular structures. Calculations were made with TURBOMOLE,^{36,37} employing Becke's three-parameter hybrid functional with Lee–Yang–Parr correlation (B3LYP),^{38,39} and polarized double- ζ valence basis sets def2-SV(P),⁴⁰ throughout (Table S4). From the obtained transitions, the spectra were simulated by superimposing Gaussians with a full width at half-maximum of 0.3

eV. Note that the solid-state absorption/PLE spectra in general overemphasize the intensity of weak bands due to the high optical thickness and nonvalidity of the Beer–Lambert law for polycrystalline sample preparations such as used for 1–5. Therefore, a better visual comparison of the calculated and measured spectra can be achieved by plotting the former ones on a log scale (Figures 2, S9, and S10). Additionally, an attempt was made to simulate the emission processes with TDDFT, similar to the route proposed by Costuas et al.⁴¹ It has already been performed and described in detail for 1.¹⁵ Following this approach, the emission energies for the respective excited state of 1–5 were obtained as singlet and triplet excitation energies $\Delta E(\text{S1}, \text{T1})_{\text{exc}}$ from the ground-state determinant calculated for the relaxed structure (Table 3). Then, the theoretical Stokes shift for singlet (fluorescence) and triplet (phosphorescence) emissions may be identified by the difference $\Delta E(\text{S0})_{\text{exc}} - \Delta E(\text{S1}, \text{T1})_{\text{exc}}$, where $\Delta E(\text{S0})_{\text{exc}}$ is the lowest excitation energy for the structural parameters optimized for the ground state.

Absorption/PL Excitation Spectra. In accordance with the visual appearance of 1–5 (from dark violet-red to nearly black polycrystals), their absorption and PL excitation (PLE) spectra extend to the red or near-infrared spectral region. The first absorption bands in the low-temperature PLE spectra,

Table 3. Calculated Data for the Optimized Structures (eV)^a

	E_{gap}	$\Delta E(\text{S0})_{\text{exc}}$	$\Delta E(\text{S1})_{\text{exc}}$	$\Delta E(\text{T1})_{\text{exc}}$	Stokes shift	
					$\Delta E(\text{S0})_{\text{exc}} - \Delta E(\text{S1})_{\text{exc}}$	$\Delta E(\text{S0})_{\text{exc}} - \Delta E(\text{T1})_{\text{exc}}$
1	2.54	1.62	1.46 ^b	1.41	0.16 ^b	0.21
2	2.79	1.87	1.57	1.56 ^b	0.30	0.31 ^b
3	3.03	2.12	1.80	1.69 ^b	0.32	0.43 ^b
4	2.36	1.45	1.33 ^b	1.28	0.11 ^b	0.16
5	2.55	1.64	1.39	1.32 ^b	0.25	0.31 ^b

^aEnergy of the HOMO–LUMO gap E_{gap} , first singlet excitation energy for the ground state $\Delta E(\text{S0})_{\text{exc}}$, first singlet and triplet excitation energies of the first excited state $\Delta E(\text{S1})_{\text{exc}}/\Delta E(\text{T1})_{\text{exc}}$, and Stokes shift for 1–5. ^bValues correspond to the assignment of the luminescence as fluorescent (1, 4) or phosphorescent (2, 3, 5) according to the experimental PL decay times.

displaying similar but sharper features as compared to the absorption spectra at 295 K, were estimated to lie at *ca.* 875, 720, 602, 1030, and 840 nm (1.42, 1.72, 2.06, 1.20, and 1.48 eV) for 1–5, respectively (Table 2). The combinations of Cu, Se (4) and Na, S (3) in the M_2TiE_6 core ($M = Cu, Ag, Na$; $E = S, Se$) thus lead to the lowest and highest energies, respectively. For all compounds, the above absorption bands are well reproduced (within *ca.* 0.2 eV) by the calculated lowest-energy singlet excitations (Tables 3 and S4). Furthermore, the whole band patterns in the absorption/PLE spectra of 1–5 measured up to *ca.* 4 eV appear to be in good agreement with the simulated spectra, as illustrated in Figures 2, 3, S9, and S10.

The character of the lowest electronic transitions (<2.75 eV) is very similar for all compounds. The nonrelaxed difference density plots (insets in Figures 2, S9, and S10) reveal a high localization within the M_2TiE_6 core (with only small “external” contributions of the π orbitals of the chalcogen phenyl groups). Mainly involved are HOMO, HOMO – 1, and LUMO; consequently, the calculated excitation energies show a linear dependence on the HOMO–LUMO gap; see Table 3. For a rationalization of the differences in excitation energies, a more detailed inspection of the frontier orbitals is justified. Their shapes and energies (Figures 4, S12, and S13; Tables S3 and

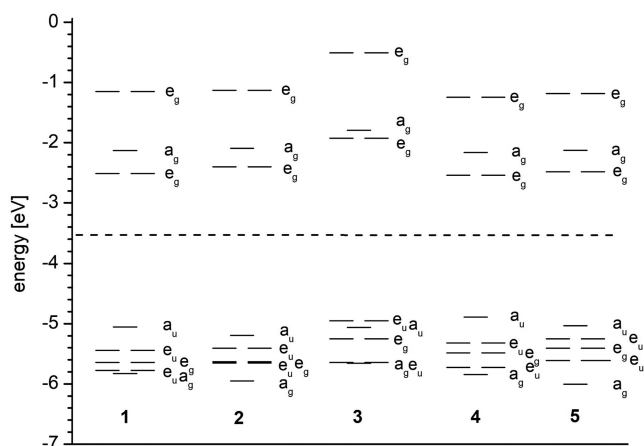


Figure 4. Calculated molecular orbital diagrams of 1–5 for the energies of the optimized structures (data taken from Table S4). The dashed line separates occupied orbitals from unoccupied ones.

S4) are very similar for homologous 1, 2, 4, and 5, reflecting the structural similarity of these compounds (all exhibiting S_6 symmetry). The sodium–titanium complex 3, including six Na-coordinated thf molecules, structurally deviates from the other compounds (see above) and comprises a reversed symmetry order for HOMO and HOMO – 1 (Figure 4, Tables S3 and S4), but with a very small energy difference of ~ 0.1 eV. Mulliken contributions of atomic orbital shells (d, p) to the frontier orbitals in 1–5 (Table 4) show that the lowest unoccupied MOs in 1–5 are largely dominated by the d orbitals of the titanium atom, with minor contributions of the chalcogen ($E = S, Se$) and side metal atoms ($M = Cu, Ag$), whereas the occupied MOs involve only the p orbitals of S and Se and the d orbitals of Cu and Ag. The copper atoms in 1 and 4 thereby contribute notably more ($\sim 8\%$) than the silver atoms ($\sim 3\%$) in 2 and 5; sodium atoms in 3 are practically not involved.

The molecular orbital diagrams (MOs) of 1–5 depict the influences of the choice of element combination on the

Table 4. Mulliken Contributions in % of Atomic Orbital Shells (d, p) with Respect to the Frontier Orbitals in 1–5^a

			1	2	3	4	5
a_g	LUMO + 1	d(M)	2.5	0.8	0.1	2.1	0.8
		d(Ti)	73.8	78.4	75.2	73.7	79.8
		p(E)	2.4	1.8	2.2	2.7	2.1
e_g	LUMO	d(M)	0.5	0.1	0	0.35	0.1
		d(Ti)	80.5	78.9	76.5	80	78.7
		p(E)	1.7	2.0	1.9	1.7	2.0
a_u	HOMO for 1, 2, 4, and 5 and HOMO – 1 for 3	d(M)	8.6	3.0	0	7.2	3.2
		d(Ti)	0	0	0	0	0
		p(E)	7.8	8.4	9.7	9.6	10.4
e_u	HOMO for 3 and HOMO – 1 for 1, 2, 4, and 5	d(M)	8.5	2.1	0	8.4	3.3
		d(Ti)	0	0	0	0	0
		p(E)	9.1	10.6	10.9	11.0	13.5

^ad(Ti) denotes the contribution of the d shell of the titanium atom, d(M) denotes that of one of the two metal atoms ($M = Cu, Ag, Na$), and p(E) denotes that of one of the p shells of the six chalcogen atoms ($E = S, Se$). The contributions of remaining shells of all of these atoms to the listed orbitals are below 1% and therefore omitted.

HOMO and LUMO and thus their effect on the HOMO–LUMO gaps and finally on the absorption onsets (Figure 4). Most striking, for 3, the LUMO is much higher in energy than for the other compounds, which results in the largest HOMO–LUMO gap among 1–5. Hence, the introduction of transition metal copper or silver into the coordination surroundings of the $[Ti(SPh)_6]^{2-}$ complex unit instead of main group element sodium results in a distinct lowering of the LUMO. Within compounds 1, 2, 4, and 5 the following trends are observed: When exchanging Cu with Ag for a given chalcogen (1 \rightarrow 2, 4 \rightarrow 5), the HOMO–LUMO gap becomes larger due to both an increase in the LUMO and a decrease in the HOMO energy. When exchanging S with Se for a given metal atom (1 \rightarrow 4, 2 \rightarrow 5), the gap becomes smaller due to an increase in the HOMO energy while the LUMO energy is almost unchanged. Whereas the last observation may be rationalized by almost unchanged atomic contributions for the LUMOs (Table 4), the energetic changes for the other cases cannot be traced back to changes in atomic contributions in an easy way. We nevertheless list the following coincidences: When exchanging Cu with Ag, the decrease in the HOMO energy comes with a decrease in the d-shell contribution of the metal atom for this orbital (see above), and the increase in the LUMO energy comes with an increase in the d-shell contributions of both the titanium and the metal M atoms.

Emission Spectra. Similar to 1, solid compounds 2–4 demonstrate strong NIR PL at temperatures below ~ 100 K whereas 5 emits with relatively low intensity even at 5 K (Figures 2 and S9–S11). The energetic positions of these bands at low temperatures follow for copper and silver complexes 1, 2, 4, and 5 the trend of the first PLE maximum (Figures 2, 3, and S11, Table 2). This means that the PL in the copper selenolate complex 4 is most red-shifted in the NIR to an energy of as low as 1205 nm (1.03 eV), followed by 5 (1075 nm/1.15 eV), 1 (1063/1.17), and 2 (885/1.40). This manifests the trend that both the absorption and PL maximum are lowered by a replacement of sulfur by selenium or silver by copper, respectively. Experimental Stokes shifts of about 0.17–0.32 eV are found to be moderate but slightly smaller for the copper complexes 1 and 4 compared to the silver complexes 2 and 5 (PL maximum relative to the first band in the absorption/PLE spectrum; Figures 2, 3, and S11, Table 2).

In contrast, the sodium–titanium complex **3** is distinguished by a much broader emission and a distinctly larger Stokes shift of about 0.77 eV, violating the energetic order suggested by the first PLE maxima. Its PL is phosphorescence with a lifetime of tens of microseconds at 20 K (Table 2), similar to the silver complex **2** which comprises a moderately faster microsecond decay. The PL lifetime of **5** amounts to 90 ns. Because it emits with a relatively low intensity even at 5 K, this decay is mainly determined by nonradiative relaxation processes. The radiative lifetime likely lies in the microsecond range. Accordingly, the PL of the second silver complex **5** was also attributed to phosphorescence.

In contrast to the silver- and sodium-containing complexes **2**, **3**, and **5**, the copper–titanium complexes **1** and **4** also remain efficient emitters at ambient temperature, with relatively high PL quantum yields, Φ_{PL} , of 9.5 and 4.8% at 295 K, respectively. In addition, their emissions decay quickly (within tens of nanoseconds at low temperatures), show the smallest Stokes shift of the five complexes (0.25 and 0.17 eV for **1** and **4**), and therefore may be ascribed to fluorescence. Referring to Φ_{PL} values at 295 K, PL efficiencies of about 30 and 10% can be estimated for **1** and **4** below 50 K.

The calculated emission energies for the relaxed singlet (**1** and **4**) and triplet (**2**, **3**, and **5**) excited states (Table 3) correspond reasonably well to the experimental data (Table 2). Although the calculations generally overestimate the emission energies by ca. 0.2–0.3 eV for **1**, **2**, **4**, and **5**, their Stokes shifts are predicted to be within 0.1 eV of the experimental values (Tables 2 and 3). A larger deviation is found for the sodium–titanium complex **3** with the calculated vs observed Stokes shift of ca. 0.42 vs 0.77 eV. Similar to the previous results,¹⁵ a correlation between the PL properties of the chalcogenolato bridged metal complexes and their structural relaxation upon photoexcitation has been revealed, in particular, that regarding the distance between the central titanium atom and its neighboring metal atoms. For the fluorescent copper complexes **1** and **4**, only moderate changes are found for both singlet and triplet excited states versus the optimized ground-state structure (Table S5). In contrast, a pronounced bond contraction along the M–Ti–M axis occurs in the excited states of the phosphorescent silver complexes **2** and **5**, mainly due to a more pronounced reduction of the M–E–Ti angle upon excitation. A different structural relaxation thus contributes to the different Stokes shifts observed for the copper- and silver–titanium compounds. The sodium–titanium complex **3** is in a certain sense difficult to compare to the copper and the silver compounds **1**, **2**, **4**, and **5**, both due to different ligands (thf vs PPh₃) and to the different character of the HOMO: e_u for **3** but a_u for the other compounds. This leads to different characters of the lowest excitations (the LUMO is e_g for all compounds): $a_u \times e_g = e_u$ for **1**, **2**, **4**, and **5** but $e_u \times e_g = 2a_u + e_u$ for **3**. However, there seems to be a correlation of the distinct destabilization of the LUMO in **3** in comparison to **1**, **2**, **4**, and **5** and the largest Stokes shift observed for this compound. Even more general, larger excitations (or larger HOMO–LUMO gaps, respectively) coincide with larger Stokes shifts (Table 3) and thus similar arguments, in particular, the gap-reducing higher d-shell contributions of Cu compared to Ag, may serve for their rationalization (Table 4).

We note that the calculation results for singlet excitations, energies and structure relaxation are presented/compared in Tables S2, S3, and S5 for the both optimized (i.e., free

molecule or gas phase) and experimentally determined (XRD) ground-state structure. Distinct differences between these structures may be mostly assigned to crystal packing effects. For instance, for all compounds the experimental solid-state structure shows a notable contraction in the M–Ti bond length (up to 19 pm in **4**) in comparison to the optimized molecular geometry. The choice of structure also has a significant impact on the calculated absolute energies of the frontier orbitals (Table S4). However, the energies of dipole active singlet transitions, which define the absorption/PLE spectra of **1**–**5**, vary only moderately for the optimized vs solid-state structures (Table S3).

SUMMARY AND CONCLUSIONS

In continuation of our work on the copper–titanium complex [Cu₂Ti(SPh)₆(PPh₃)₂],¹⁵ we obtained a series of NIR-luminescent trinuclear chalcogenolato bridged metal complexes of the same type [M₂Ti(EPh)₆(PPh₃)₂] with M = Ag, Cu; E = S, Se and of a closely related structure [Na(thf)₃]₂[Ti(SPh)₆]. All of these compounds absorb in the red or NIR spectral range and show NIR photoluminescence with the emission maxima at ca. 880–1200 and 920–1240 nm at low (<100 K) and elevated (150–295 K) temperatures, respectively. Quantum chemical calculations have been performed (DFT and TDDFT) in order to gain an understanding of how the elemental composition determines the electronic situation and optical performance of the complexes.

The optical properties in the low-energy region (<2.7 eV) of ionic [Na(thf)₃]₂[Ti(SPh)₆] are almost solely determined by the complex anion comprising sulfur p- to titanium d-orbital charge-transfer excitations. Upon a formal substitution of the sodium atoms by copper or silver atoms in the metal position M (accompanied by an exchange of thf by triphenylphosphine ligands) the compounds become more covalent as indicated by distinctly smaller M–S bond distances as well as shorter nonbonding M···M distances. The lowest excitations are pure HOMO–LUMO transitions, and thus the excitation energies decrease with decreasing HOMO–LUMO gaps from Na via Ag to Cu, coinciding with increasing d-shell contributions to the frontier orbitals. Although these contributions are moderate, they seem to have a distinct influence on the optical performance of the compounds.

With respect to the emission properties, Stokes shifts are experimentally found to be largest (0.77 eV) in [Na(thf)₃]₂[Ti(SPh)₆], intermediate (0.32 and 0.33 eV) in the two silver complexes, and smallest (0.17 and 0.25) in the complexes with copper in the metal position M. These trends are reproduced by the calculations. The size of the shifts in principle increases with the size of the excitation energies and thus with the size of the HOMO–LUMO gaps. More significant, the two copper complexes differ in terms of the PL stability and PL decay times from the silver analogues and [Na(thf)₃]₂[Ti(SPh)₆]. Thus, [Cu₂Ti(EPh)₆(PPh₃)₂] (E = S, Se) retains high PL efficiencies of 9.5 and 4.8% at ambient temperature, which is remarkable with regard to their low emission energies (1240 nm/1.0 eV and 1090 nm/1.14 eV at 295 K). In addition, these two complexes reveal nanosecond-fast decay indicating fluorescence. For all other complexes, the PL is quenched at least above 150 K and the microsecond-long emission can be ascribed to phosphorescence.

This distinct PL behavior of the two copper complexes in comparison to the other three compounds cannot be

completely rationalized on the basis of the theoretical data. In particular, the differences between the copper complexes and the silver complexes indicate the existence of different relaxation pathways, which might have a significant influence on their PL performance.

EXPERIMENTAL SECTION

Synthesis. Standard Schlenk techniques were employed throughout the syntheses using a double-manifold vacuum line with high-purity dry nitrogen (99.9994%) and an MBraun glovebox with high-purity dry argon (99.9990%). Solvents diethyl ether (Et₂O), tetrahydrofuran (THF), and toluene were dried over sodium benzophenone and distilled under nitrogen. Anhydrous dichloromethane (CH₂Cl₂; H₂O < 0.005%) obtained from Aldrich was degassed, freshly distilled, and stored over molecular sieves under nitrogen. Anhydrous CuCl and AgCl were obtained from Sigma-Aldrich. CuCl was subsequently washed with HCl, CH₃OH, and diethyl ether to remove traces of CuCl₂ and dried under vacuum. TiCl₄·2THF, [AgCl(PPh₃)₃],⁴² [(PPh₃)₂CuSPh]₂,⁴³ AgSPh,⁴⁴ and LiSPh⁴⁵ were prepared according to literature procedures. PPh₃ obtained from Sigma-Aldrich was recrystallized in ethanol before use. NaEPh (E = S, Se) has been prepared by the reduction of (PhE)₂ with Na in NH₃/DME.

Solution ¹H and ¹³C NMR data of 1–5 are not given, as changes in color accompanied by strong shifts in absorption maxima and the formation of precipitates indicate at least partial decomposition of the complexes when redissolved.

[Cu₂Ti(SPh)₆(PPh₃)₂] (1) was prepared according to ref 15.

[Ag₂Ti(SPh)₆(PPh₃)₂] (2). [TiCl₄(thf)₂] (169 mg, 0.505 mmol) was reacted with NaSPh (274 mg, 2.07 mmol) in 10 mL of thf to give an intensely red, slightly turbid solution. This was centrifuged, and the solid residue was washed once with another 10 mL of thf. After unification, this reaction solution was added to a solution of AgSPh (239 mg, 1.1 mmol) dissolved with PPh₃ (530 mg, 2.02 mmol) in 10 mL of CH₂Cl₂. Dark-red crystals of 2 started to form after 1 h and were separated by decantation from the mother liquor after 2 days; then they were washed two times with 10 mL of cold thf (−75 °C) and once with 10 mL of Et₂O (−40 °C) to yield 480 mg (65.8%) of 2 after drying in vacuo. (2) C₇₂H₆₀Ag₂P₂S₆Ti (1443.19): calcd C 59.92, H 4.19, S 13.33; found C 59.89, H 4.45, S 12.66%.

[Na(thf)₃]₂[Ti(SPh)₆] (3). [TiCl₄(thf)₂] (169 mg, 0.505 mmol) was reacted with NaSPh (414 mg, 3.13 mmol) in 15 mL of thf to yield a dark-red solution with a red microcrystalline precipitate within one night. After the addition of 10 mL of dme, NaCl was separated by centrifugation from the solution, the latter one mixed with 20 mL of Et₂O and stored in a freezer (−42 °C). Dark-red crystals of 3 are formed within one night; they were separated by decantation from the mother liquor and washed two times with a 1:1 mixture of thf/Et₂O at −75 °C to give, after subsequent drying in a stream of dry N₂ and briefly in vacuo (~10 mbar), 310 mg (45.3%) of 3. (3) C₆₀H₇₈Na₂O₆S₆Ti (1181.49): calcd C 60.99, H 6.65, S 16.28; found C 59.89, H 6.35, S 16.31%. The complex gradually decomposes in vacuo (~1 mbar) by the cleavage of thf.

[Cu₂Ti(SePh)₆(PPh₃)₂] (4). [TiCl₄(thf)₂] (150 mg, 0.45 mmol) and CuCl (89 mg, 0.9 mmol) were dissolved with PPh₃ (295 mg, 1.13 mmol) in 15 mL of thf. This orange-yellow solution was then cooled to −45 °C, and PhSeSiMe₃ (0.56 mL, 2.93 mmol) was added. Upon warming up to rt with stirring, the solution gradually turned dark red. After 1 day, the solvent was removed and the residue was dissolved in 10 mL of thf. A black crystalline precipitate of 4 was formed in a few days upon keeping the solution first at rt and then in a refrigerator. The supernatant solution was then decanted, and the crystals were washed two times with 10 mL of cold thf (−75 °C) and once with 10 mL of Et₂O (rt) to yield 230 mg (31.3%) of 4 after drying in vacuo. The addition of 20 mL of Et₂O to the decanted solution gives upon standing in the refrigerator another 80 mg to result in a total yield of 310 mg (42.1%). (4) C₇₂H₆₀Cu₂P₂Se₆Ti (1635.91): calcd C 52.86, H 3.70; found C 53.31, H 4.02%.

[Ag₂Ti(SePh)₆(PPh₃)₂] (5). First, AgCl (143 mg, 1.0 mmol) was reacted with PPh₃ (787 mg, 3.02 mmol) in 15 mL of thf for 3 days to give an almost-white suspension. The addition of PhSeSiMe₃ (252 mg, 1.1 mmol) yielded in several hours a clear yellow solution. The solvent and volatile reaction products were then removed by vacuum condensation, and the greasy yellow residue was redissolved in 10 mL of thf. In a second flask, [TiCl₄(thf)₂] (169 mg, 0.505 mmol) was reacted with NaSePh (364 mg, 2.07 mmol) in 10 mL of thf to give an intensely red, slightly turbid solution. This was centrifuged after 2 h, and the solid residue was washed once with another 10 mL of thf. After unification, both reaction solutions were mixed, attaining a nearly black color. This solution was again reduced by vacuum condensation to a total of 10 mL. Upon addition of 10 mL of Et₂O, dark-red crystals of 5 formed within 4 days, which were separated by decantation from the mother liquor and washed two times with 10 mL of cold thf (−75 °C) and once with 10 mL of Et₂O (−40 °C) to yield 400 mg (46%) of 5 after drying in vacuo. Upon repetition of the reaction procedures, we sometimes observed the cocrystallization of yellow [Ag₄Se(SePh)₁₂(PPh₃)₈], which seemed to preferentially occur when we tried to optimize yields by applying higher amounts of Et₂O, a lower crystallization temperature, and longer crystallization times.⁴⁶ (5) C₇₂H₆₀Ag₂P₂Se₆Ti (1724.56): calcd C 50.15, H 3.51; found C 50.41, H 3.87%.

Crystallography. Because of the air and moisture sensitivity of the compounds, crystals suitable for single-crystal X-ray diffraction were selected in perfluoroalkylether oil and mounted quickly into the diffractometer equipped with an Oxford Cryosystems cooler. Single-crystal XRD data of 1–5 were collected using Mo K α radiation (λ = 0.71073 Å) generated by a microfocus sealed X-ray tube (Mo Genix 3D) with multilayer optics on a STOE STADI Vari (Pilatus Hybrid Pixel Detector 300 K). Raw intensity data were collected and treated with STOE X-Area software, version 1.82. Data for all compounds were corrected for Lorentz and polarization effects. With implemented program STOE LANA, interframe scaling of the data sets was carried out, along with multiscan absorption corrections by the scaling of reflection intensities.⁴⁷ Within Olex2,⁴⁸ the structures were solved with the ShelXT⁴⁹ structure solution program involving intrinsic phasing and refined with the ShelXL refinement package using least-squares minimization. Molecular diagrams were prepared using Diamond.⁵⁰

In 1–5, all Ag, Cu, Ti, Se, S, O, P, and C atoms were refined with anisotropic displacement parameters, while H atoms were computed and refined using a riding model, with the isotropic temperature factor equal to 1.2 times the equivalent temperature factor of the atom to which they are linked. In 1 and 2, the C atoms of the phosphine phenyl ring were refined with a split model of site disorder. In 3, the C atoms of thf were refined with this model. Lattice solvent molecules were identified within all structures. These are located at special positions and could not be adequately refined due to disorder. Therefore, for correction, the solvent-masking routine implemented in Olex2 was used, which is based on the method described by van der Sluis and Spek.⁵¹ The following corrections have been applied:

1. a total of 90 electrons in a potential solvent-accessible volume of ~365 Å³;
2. a total of 208 electrons in a potential solvent-accessible volume of ~379 Å³ (in the presence of CH₂Cl₂);
3. a total of 98 electrons in a potential solvent-accessible volume of ~347 Å³;
4. a total of 104 electrons in a potential solvent-accessible volume of ~425 Å³;
5. a total of 27 electrons in a potential solvent-accessible volume of ~309 Å³ (vacuum-dried crystals).

X-ray powder diffraction patterns (XRD) for 1–5 (powder of crystals) were measured at rt on a STOE STADI P diffractometer (Cu K α 1 radiation, germanium monochromator, Debye–Scherrer geometry, Mythen 1K detector) in sealed glass capillaries. The theoretical powder diffraction patterns were calculated on the basis of the atom coordinates obtained from single-crystal X-ray analysis (180 K) by using the STOE WinXPow program package.⁵²

Physical Measurements. C, H, and S elemental analyses were performed on an Elementar vario Micro cube instrument.

Solid-state UV–vis absorption spectra of 1–5 were recorded on a PerkinElmer Lambda 900 spectrophotometer equipped with a Labsphere integrating sphere in transmission and reflection modes for samples which were prepared as micrometer-sized crystalline powders dispersed in a Nujol layer between two quartz plates.

Photoluminescence (PL) measurements were performed on a Horiba JobinYvon Fluorolog-3 spectrometer equipped with a Hamamatsu R5509 vis-NIR photomultiplier (~300–1400 nm) and an optical close-cycle cryostat (Leybold) for measurements at cryogenic temperatures down to 16 K. Compound 5 was measured in a pulse tube cryostat (Cryomech) from 5 to 150 K. The same sample preparations as for absorption measurements were applied. The emission spectra were corrected for the wavelength-dependent response of the spectrometer and detector (in relative photon flux units). Emission decay traces were recorded by connecting the photomultiplier to an oscilloscope (with a 50 Ω or larger load depending on the time scale) and using a N₂ laser for pulsed excitation at 337 nm (~2 ns, ~5 μ J per pulse). The PL quantum yield of 4 excited at 500 nm was measured at ambient temperature according to de Mello et al.⁵³ using a 10 cm integrating sphere out of optical PTFE with low autoluminescence (Berghof GmbH), which was installed in the sample chamber of the Fluorolog-3. The accuracy was estimated to be $\pm 10\%$.

Quantum Chemical Calculations. Calculations were made with TURBOMOLE,^{36,54} employing Becke's three-parameter hybrid functional with Lee–Yang–Parr correlation (B3LYP)^{55,56} and polarized double- ζ valence basis sets def2-SV(P)⁵⁷ within the RI-J approximation⁵⁸ throughout. Electronic excitations were obtained from time-dependent calculations.⁵⁹ Stokes shifts were calculated as the differences in the lowest excitation energies for the ground state and the excited-state structure. Contributions of atomic to molecular orbitals were obtained from Mulliken population analyses.⁶⁰ The character of the electronic excitation bands was visualized using the nonrelaxed transition densities as described previously.⁶¹

■ ASSOCIATED CONTENT

SI Supporting Information

The Supporting Information is available free of charge at <https://pubs.acs.org/doi/10.1021/acs.inorgchem.1c00829>.

Crystallographic data, molecular structures, XRD powder patterns, absorption and PL spectra, and comprehensive data of quantum chemical calculations (PDF)

Accession Codes

CCDC 2044048–2044052 contain the supplementary crystallographic data for this paper. These data can be obtained free of charge via www.ccdc.cam.ac.uk/data_request/cif, or by emailing data_request@ccdc.cam.ac.uk, or by contacting The Cambridge Crystallographic Data Centre, 12 Union Road, Cambridge CB2 1EZ, UK; fax: +44 1223 336033.

■ AUTHOR INFORMATION

Corresponding Author

Andreas Eichhöfer – Institut für Nanotechnologie, Karlsruher Institut für Technologie (KIT), 76344 Eggenstein-Leopoldshafen, Germany; Lehn Institute of Functional Materials, Sun Yat-Sen University, Guangzhou 510275, China; Karlsruhe Nano Micro Facility (KNMF), 76344 Eggenstein-Leopoldshafen, Germany; orcid.org/0000-0002-3412-6280; Phone: 49-(0)721-608-26371; Email: andreas.eichhoefer@kit.edu

Authors

Sergei Lebedkin – Institut für Nanotechnologie, Karlsruher Institut für Technologie (KIT), 76344 Eggenstein-Leopoldshafen, Germany

Florian Weigend – Institut für Nanotechnologie, Karlsruher Institut für Technologie (KIT), 76344 Eggenstein-Leopoldshafen, Germany; Fachbereich Chemie, Philipps-Universität Marburg, 35032 Marburg, Germany; orcid.org/0000-0001-5060-1689

Complete contact information is available at: <https://pubs.acs.org/doi/10.1021/acs.inorgchem.1c00829>

Author Contributions

A.E. was responsible for synthesis and characterization; S.L., for PL measurements; and F.W., for DFT and TDDFT calculations.

Notes

The authors declare no competing financial interest.

■ ACKNOWLEDGMENTS

This work was supported by the Karlsruhe Institute of Technology (KIT, Campus Nord) and the Karlsruhe Nano-Micro-Facility (KNMF). The authors thank S. Stahl for carrying out the elemental analysis. A.E. thanks A. K. Powell for generous support.

■ REFERENCES

- (1) Bergmann, L.; Friedrichs, J.; Mydlak, M.; Baumann, T.; Nieger, M.; Bräse, S. Outstanding luminescence from neutral copper(I) complexes with pyridyl-tetrazolate and phosphine ligands. *Chem. Commun.* **2013**, *49*, 6501–6503.
- (2) Igawa, S.; Hashimoto, M.; Kawata, I.; Yashima, M.; Hoshino, M.; Osawa, M. Highly efficient green organic light-emitting diodes containing luminescent tetrahedral copper(I) complexes. *J. Mater. Chem. C* **2013**, *1*, 542–551.
- (3) Wang, Y.-M.; Teng, F.; Hou, Y.-B.; Xu, Z.; Wang, Y.-S.; Fu, W.-F. Copper(I) complex employed in organic light-emitting electrochemical cells: Device and spectra shift. *Appl. Phys. Lett.* **2005**, *87*, 233512.
- (4) Cariati, E.; Lucenti, E.; Botta, C.; Giovannella, U.; Marinotto, D.; Righetto, S. Cu(I) hybrid inorganic–organic materials with intriguing stimuli responsive and optoelectronic properties. *Coord. Chem. Rev.* **2016**, *306*, 566–614.
- (5) Yam, V. W.-W.; Lo, K. K.-W.; Fung, W. K.-M.; Wang, C.-R. Design of luminescent polynuclear copper(I) and silver(I) complexes with chalcogenides and acetylides as the bridging ligands. *Coord. Chem. Rev.* **1998**, *171*, 17–41.
- (6) Ford, P. C.; Vogler, A. Photochemical and Photophysical Properties of Tetranuclear and Hexanuclear Clusters of Metals with d¹⁰ and s² Electronic Configurations. *Acc. Chem. Res.* **1993**, *26*, 220–226.
- (7) Bergmann, L.; Hedley, G. J.; Baumann, T.; Bräse, S.; Samuel, D. W. Direct observation of intersystem crossing in a thermally activated delayed fluorescence copper complex in the solid state. *Sci. Adv.* **2016**, *2*, e1500889.
- (8) Hofbeck, T.; Monkowius, U.; Yersin, H. Highly Efficient Luminescence of Cu(I) Compounds: Thermally Activated Delayed Fluorescence Combined with Short-Lived Phosphorescence. *J. Am. Chem. Soc.* **2015**, *137*, 399–404.
- (9) Knorr, M.; Bonnot, A.; Lapprand, A.; Khatyr, A.; Strohmman, C.; Kubicki, M.; Rousselin, Y.; Harvey, P. D. Reactivity of CuI and CuBr toward Dialkyl Sulfides RSR: From Discrete Molecular Cu₄I₄S₄ and Cu₈I₈S₈ Clusters to Luminescent Copper(I) Coordination Polymers. *Inorg. Chem.* **2015**, *54* (8), 4076–4093.
- (10) Hupp, B.; Schiller, C.; Lenczyk, C.; Stanoppi, M.; Edkins, K.; Lorbach, A.; Steffen, A. Synthesis, Structures, and Photophysical

Properties of a Series of Rare Near-IR Emitting Copper(I) Complexes. *Inorg. Chem.* **2017**, *56*, 8996–9008.

(11) Langer, R.; Yadav, M.; Weinert, B.; Fenske, D.; Fuhr, O. Luminescence in Functionalized Copper Thiolate Clusters – Synthesis and Structural Effects. *Eur. J. Inorg. Chem.* **2013**, *2013*, 3623–3631.

(12) Yue, C.; Yan, C.; Feng, R.; Wu, M.; Chen, L.; Jiang, M.; Hong, M. A Polynuclear d^{10} – d^{10} Metal Complex with Unusual Near-Infrared Luminescence and High Thermal Stability. *Inorg. Chem.* **2009**, *48*, 2873–2879.

(13) Yang, X.-X.; Issac, I.; Lebedkin, S.; Kühn, M.; Weigend, F.; Fenske, D.; Fuhr, O.; Eichhöfer, A. Red-luminescent biphosphine stabilized $Cu_{12}S_6$ cluster molecules. *Chem. Commun.* **2014**, *50*, 11043–11045.

(14) Eichhöfer, A.; Buth, G.; Kühn, M.; Weigend, F. Luminescence in Phosphine-Stabilized Copper Chalcogenide Cluster Molecules—A Comparative Study. *Inorg. Chem.* **2015**, *54*, 9413–9422.

(15) Kühn, M.; Lebedkin, S.; Weigend, F.; Eichhöfer, A. Optical Properties of Trinuclear Metal Chalcogenolate Complexes — Room Temperature NIR Fluorescence in $[Cu_2Ti(SPh)_6(PPH_3)_2]$. *Dalton Trans.* **2017**, *46*, 1502–1509.

(16) Wang, L.-S.; Sheng, T.-L.; Wang, X.; Chen, D.-B.; Hu, S.-M.; Fu, R.-B.; Xiang, S.-C.; Wu, X.-T. Self-Assembly of Luminescent Sn(IV)/Cu/S Clusters Using Metal Thiulates as Metalloligands. *Inorg. Chem.* **2008**, *47*, 4054–4059.

(17) Wang, X.; Sheng, T.-L.; Fu, R.-B.; Hu, S.-M.; Xiang, S.-C.; Wang, L.-S.; Wu, X.-T. Assembly of a Heterometallic Polynuclear SnIV-CuI Cluster Based on $Sn(edt)_2$ ($edt = \text{Ethane-1,2-dithiolate}$) as a Metalloligand. *Inorg. Chem.* **2006**, *45*, 5236–5238.

(18) Eichhöfer, A.; Jiang, J.; Lebedkin, S.; Fenske, D.; McDonald, D. G.; Corrigan, J. F.; Su, C.-Y. A ternary Cu–Sn–S cluster complex— $(NBu_4)[Cu_{19}S_{28}(SnPh)_{12}(PEt_2Ph)_3]$. *Dalton Trans.* **2012**, *41*, 3321–3327.

(19) Xiang, H.; Cheng, J.; Ma, X.; Zhou, X.; Chruma, J. J. Near-infrared phosphorescence: materials and applications. *Chem. Soc. Rev.* **2013**, *42*, 6128–6185.

(20) Amoroso, A. J.; Pope, S. J. A. Using lanthanide ions in molecular bioimaging. *Chem. Soc. Rev.* **2015**, *44*, 4723–4742.

(21) Zhao, Q.; Huang, C.; Li, F. Phosphorescent heavy-metal complexes for bioimaging. *Chem. Soc. Rev.* **2011**, *40*, 2508–2524.

(22) Kumar, A.; Riman, R. E.; Brennan, J. G. NIR Emission from Molecules and Clusters with Lanthanide-Chalcogen Bonds. *Coord. Chem. Rev.* **2014**, *273–274*, 111–124.

(23) Wu, W.; Zhang, X.; Kornienko, A. Y.; Kumar, G. A.; Yu, D.; Emge, J.; Riman, R. E.; Brennan, J. G. Efficient NIR emission from Nd, Er, and Tm complexes with fluorinated selenolate ligands. *Inorg. Chem.* **2018**, *57*, 1912–1918.

(24) Bünzli, J.-C. On the Design of Highly Luminescent Lanthanide Complexes. *Coord. Chem. Rev.* **2015**, *293–294*, 19–47.

(25) Caspar, J. V.; Meyer, T. J. Application of the energy gap law to nonradiative, excited-state decay. *J. Phys. Chem.* **1983**, *87*, 952–957.

(26) Doffek, C.; Wahsner, J.; Kreidt, E.; Seitz, M. Breakdown of the Energy Gap Law in Molecular Lanthanoid Luminescence: The Smallest Energy Gap is Not Universally Relevant for Nonradiative Deactivation. *Inorg. Chem.* **2014**, *53*, 3263–3265.

(27) Andrushko, V.; Sommer, H.; Himmel, D.; Fenske, D.; Eichhöfer, A. Syntheses, Structures, and Properties of Trinuclear Copper(I)/Titanium(IV) Thiolate Complexes. *Eur. J. Inorg. Chem.* **2011**, *2011*, 3102–3110.

(28) In ref 27, the space group of **1** was determined to be $R\bar{3}$ without an inversion center at the titanium atoms.

(29) Bechlars, B.; Feuerhake, R.; Fenske, D. Synthesen und Kristallstrukturen neuer chalcogenido-verbrückter Niob-Kupfer-Cluster. *Z. Anorg. Allg. Chem.* **2007**, *633*, 2603–2613.

(30) Eichhöfer, A.; Andrushko, V.; Bodenstein, T.; Fink, K. Trinuclear Early/Late-Transition-Metal Thiolate Complexes. *Eur. J. Inorg. Chem.* **2014**, *2014*, 3510–3520.

(31) Ball, J. M.; Boorman, P. M.; Fait, J. F.; Ziegler, T. Synthesis, X-Ray Crystal Structure, and Electronic Structure of a Trinuclear WCu₂

Cluster containing a Hexathiolato Tungsten(IV) Core. *J. Chem. Soc., Chem. Commun.* **1989**, 722–723.

(32) Leverd, P. C.; Lance, M.; Nierlich, M.; Vigner, J.; Ephritikhine, M. Synthesis and Crystal Structure of Homoleptic Uranium Hexathiolates: $[NEt_2H_2]_2[U(SPh)_6]$ and $[(Ph_3P)Cu(\mu-SPh)_3U(\mu-SPh)_3Cu(PPH_3)]$. *J. Chem. Soc., Dalton Trans.* **1994**, 3563–3567.

(33) Boorman, P. M.; Kraatz, H. B.; Parvez, M.; Ziegler, T. Synthesis, Characterization and Electronic Structure of Trinuclear Complexes possessing a Hexathiatomolybdenum(IV) or Hexaselenolato-tungsten(IV) Core. *J. Chem. Soc., Dalton Trans.* **1993**, 433–439.

(34) Glaser, T.; Bill, E.; Weyhermüller, T.; Meyer-Klaucke, W.; Wieghardt, K. Sn(III) and Ge(III) in the Thiophenolato-Bridged Complexes $[LFeSnFeL]^{n+}$ and $[LFeGeFeL]^{n+}$ ($n = 2, 3$; $L = 1,4,7$ -(4-tert-Butyl-2-mercaptobenzyl)-1,4,7-triazacyclononane). *Inorg. Chem.* **1999**, *38*, 2632–2642.

(35) Optical absorption measurements in solution are not shown, as the changes in color, strong shifts of absorption maxima, and formation of precipitates indicated at least partial decomposition of 2–5 in solution.

(36) TURBOMOLE, version 7.4; TURBOMOLE is a development of the University of Karlsruhe and the Forschungszentrum Karlsruhe 1989–2007, TURBOMOLE GmbH, 2019.

(37) Furche, F.; Ahlrichs, R.; Hättig, C.; Klopper, W.; Sierka, M.; Weigend, F. Turbomole. *Wiley Interdiscip. Rev.: Comput. Mol. Sci.* **2014**, *4*, 91–100.

(38) Lee, C.; Yang, W.; Parr, R. G. Development of the Colle-Salvetti correlation-energy formula into a functional of the electron density. *Phys. Rev. B: Condens. Matter Mater. Phys.* **1988**, *37*, 785–789.

(39) Becke, A. D. J. Density-functional thermochemistry. III. The role of exact exchange. *J. Chem. Phys.* **1993**, *98*, 5648–5652.

(40) Weigend, F.; Ahlrichs, R. Balanced basis sets of split valence, triple zeta valence and quadruple zeta valence quality for H to Rn: Design and assessment of accuracy. *Phys. Chem. Chem. Phys.* **2005**, *7*, 3297–3305.

(41) Costuas, K.; Garreau, A.; Bulou, B.; Fontaine, B.; Cuny, J.; Gautier, R.; Mortier, M.; Molard, Y.; Duvail, J.-L.; Faulques, E.; Cordier, S. Combined theoretical and time-resolved photoluminescence investigations of $[Mo_6Br_8Br_6]^{2-}$ metal cluster units: evidence of dual emission. *Phys. Chem. Chem. Phys.* **2015**, *17*, 28574–28585.

(42) Sanghani, D. V.; Smith, P. J.; Allen, D. W.; Taylor, B. F. A Reinvestigation of some Triphenylphosphine-Silver Halide Complexes and their Reaction with Stannous Chloride: ^{119}Sn Mössbauer and ^{31}P FT NMR Studies. *Inorg. Chim. Acta* **1982**, *59*, 203–206.

(43) Dance, I. G.; Guernsey, P. J.; David, A.; Scudder, R. L. Planar bridging thiolate in $(Ph_3P)_2Cu(\mu-SPh)_2Cu(PPH_3)_2$. *Inorg. Chem.* **1983**, *22*, 2883–2887.

(44) Dance, I. G.; Fisher, K. J.; Herath Banda, R. M.; Scudder, M. L. Layered Structure of crystalline compounds silver thiulates (AgSR). *Inorg. Chem.* **1991**, *30*, 183–187.

(45) Köster, R.; Seidel, G.; Boese, R. 9-(Organothio)-9-borabicyclo-[3.3.1]nonane — Herstellung und Charakterisierung. *Chem. Ber.* **1988**, *121*, 1137–1142.

(46) Nayek, H. P.; Massa, W.; Dehnen, S. Presence or Absence of a Central Se Atom in Silver Selenide/Selenolate Clusters with Halite Topology. *Inorg. Chem.* **2010**, *49*, 144–149.

(47) Koziskova, J.; Hahn, F.; Richter, J.; Kozisek, J. Comparison of different absorption corrections on the model structure of tetrakis(μ_2 -acetato)-diaqua-di-copper(II). *Acta Chim. Slov.* **2016**, *9* (2), 136–140.

(48) Dolomanov, O. V.; Bourhis, L. J.; Gildea, R. J.; Howard, J. A. K.; Puschmann, H. OLEX2: a complete structure solution, refinement and analysis program. *J. Appl. Crystallogr.* **2009**, *42*, 339–341.

(49) Sheldrick, G. M.; SHELXTL 6.14: An Integrated System for Solving, Refining, and Displaying Crystal Structures from Diffraction Data; BrukerAXS Inc., Madison, WI, 2003.

(50) Diamond, version 2.1d; Brandenburg, K. Crystal and Molecular Structure Visualization. Crystal Impact GbR, 1996–2000.

(51) van der Sluis, P.; Spek, A. L. BYPASS: an effective method for the refinement of crystal structures containing disordered solvent

regions. *Acta Crystallogr., Sect. A: Found. Crystallogr.* **1990**, *A46*, 194–201.

(52) STOE. *WinXPOW, Software for Advanced Powder Diffraction Analysis*; STOE & Cie GmbH: Darmstadt, 2000.

(53) de Mello, J. C.; Wittmann, H. F.; Friend, R. H. An improved experimental determination of external photoluminescence quantum efficiency. *Adv. Mater.* **1997**, *9*, 230.

(54) Furche, F.; Ahlrichs, R.; Hättig, C.; Klopper, W.; Sierka, M.; Weigend, F. Turbomole. *Wiley Interdiscip. Rev.: Comput. Mol. Sci.* **2014**, *4*, 91–100.

(55) Lee, C.; Yang, W.; Parr, R. G. Development of the Colle-Salvetti correlation-energy formula into a functional of the electron density. *Phys. Rev. B: Condens. Matter Mater. Phys.* **1988**, *37*, 785–789.

(56) Becke, A. D. J. Density-functional thermochemistry. III. The role of exact exchange. *J. Chem. Phys.* **1993**, *98*, 5648–5652.

(57) Weigend, F.; Ahlrichs, R. Balanced basis sets of split valence, triple zeta valence and quadruple zeta valence quality for H to Rn: Design and assessment of accuracy. *Phys. Chem. Chem. Phys.* **2005**, *7*, 3297–3305.

(58) Weigend, F. Accurate Coulomb-fitting basis sets for H to Rn. *Phys. Chem. Chem. Phys.* **2006**, *8*, 1057–1065.

(59) Bauernschmitt, R.; Ahlrichs, R. Treatment of electronic excitations within the adiabatic approximation of time dependent density functional theory. *Chem. Phys. Lett.* **1996**, *256*, 454–464.

(60) Mulliken, R. S. Electronic Population Analysis on LCAO-MO Molecular Wave Functions. I. *J. Chem. Phys.* **1955**, *23*, 1833–1840.

(61) Kühn, M.; Weigend, F. Phosphorescence lifetimes of organic light-emitting diodes from two-component time-dependent density functional theory. *J. Chem. Phys.* **2014**, *141*, 224302.